Optics Communications 437 (2019) 104–109

Contents lists available at ScienceDirect

Optics Communications

journal homepage: www.elsevier.com/locate/optcom

Characterizing the ellipticity of an isolated attosecond pulse

Chunyang Zhai, Yinfu Zhang, Qingbin Zhang *

Wuhan National Laboratory for Optoelectronics and School of Physics, Huazhong University of Science and Technology, Wuhan 430074, China

ARTICLE INFO

Keywords:
Attosecond pulse
Elliptically polarized
Photoelectron momentum distribution

ABSTRACT

We propose and theoretically demonstrate a single-shot measurement method to measure the ellipticity of an isolated attosecond pulse (IAP). By solving the time-dependent Schrödinger equation, we calculate the photoelectron momentum distributions (PMDs) from strong field ionization of argon in an arbitrary polarized IAP streaked with a linearly polarized infrared pulse. It is shown that the ellipticity of the IAP is encoded in the PMDs. A linear relation between the angular shift of the three main lobes of the PMDs and the ellipticity of the IAP is obtained, which provides an efficient and robust way for characterizing the ellipticity of the IAP.

1. Introduction

The recent developments in ultrafast optics have made remarkable advances in the field of attosecond science [1–8]. In the past two decades, the generation of isolated attosecond pulses (IAPs) through the process of high harmonic generation (HHG) provides formidable tools for the investigation of many important physical processes on attosecond timescale [2,3,9–13]. The IAP has opened the path to track the electron dynamics in atomic, molecular and solid-state physics or even follow a chemical reaction. For instance, by using the newly developed tools of attosecond metrology, one can experimentally observe the electron tunneling in atoms with sub-femtosecond temporal resolution [14], and probe the temporal evolution of bound or quasibound electron wave packets in atoms [15], and so on.

Nowadays, the circularly or/and elliptically polarized HHG and attosecond pulses have been generated in experiment and attracts many interests [16–20], owing to the broad application of the processes in strong-field physics [21–29]. The circularly and elliptically polarized attosecond pulses have many potential applications, e.g., it enables precision differential measurements of circular dichroism of molecules [16,24], and allows to create attosecond quantum electron currents and attosecond magnetic field pulses inside molecules [25], etc. Consequently, the circularly and elliptically polarized attosecond pulses recently are of considerable interest. On the other hand, although many schemes have been proposed for the production of the IAP with polarization from linear through elliptical to circular [18,20], it faces formidable challenge to characterize the ellipticity of an IAP. Up to now, the temporal envelope (i.e., the pulse duration) of the linearly polarized IAP has been successfully characterized in experiment using phase retrieval and attosecond streaking techniques [9,10,12,13]. And a strategy to characterize the carrier envelope phase (CEP) of the circularly polarized IAP using the angular streaking technique has also been proposed in theory [30,31]. Measuring the ellipticity of the IAP based on a set of reflection polarizers is often limited by the narrow bandwidth in photon energy range and low efficiency [22,32]. Recently, two alternative methods have also been developed. Chen et al. [32] proposed to reconstruct the coherent light fields using the photoelectron interferogram from a copper surface. On the other hand, Jiménez-Galán et al. [33] theoretically proposed to record the polarization state of an XUV light by analyzing the asymmetry of the one-photon spectrum generated in a hydrogen atom. These approaches, however, require one to scan the IR-XUV time delay in attosecond time interval and need multi-shot measurement in experiment.

In this work, we theoretically demonstrate a single-shot measurement method to measure the ellipticity of an IAP with the photoelectron momentum distributions (PMDs). In our method, target atom is ionized with the two-color laser field synthesized by an arbitrary polarized IAP and a linearly polarized infrared (IR) pulse. By adjusting the ellipticity of the IAP from linear to circular polarization, the main lobes of the PMD show clearly angular shift. Then from the angular resolved PMD, one can retrieve the ellipticity of the IAP.

2. Theoretical model

In order to demonstrate our method, we calculate the PMD from strong field ionization of argon in the two-color laser fields by solving the two-dimensional time-dependent Schrödinger equation (2D-TDSE) [34] in length gauge (atomic units are used unless otherwise stated),

$$i\frac{\partial\Psi(\mathbf{r},t)}{\partial t}=[-\frac{1}{2}\nabla^2+V(\mathbf{r})+\mathbf{r}\cdot\mathbf{E}(t)]\Psi(\mathbf{r},t), \quad (1)$$

where, $\Psi(\mathbf{r},t)$ represents the wave function of system, $\mathbf{r}$ is the position operator of electron. $V(\mathbf{r})=-1/\sqrt{\mathbf{r}^2+a^2}$ is the soft-core potential,

* Corresponding author.
E-mail address: zhangqingbin@hust.edu.cn (Q. Zhang).

https://doi.org/10.1016/j.optcom.2018.12.047
Received 22 August 2018; Received in revised form 22 November 2018; Accepted 12 December 2018
Available online 19 December 2018

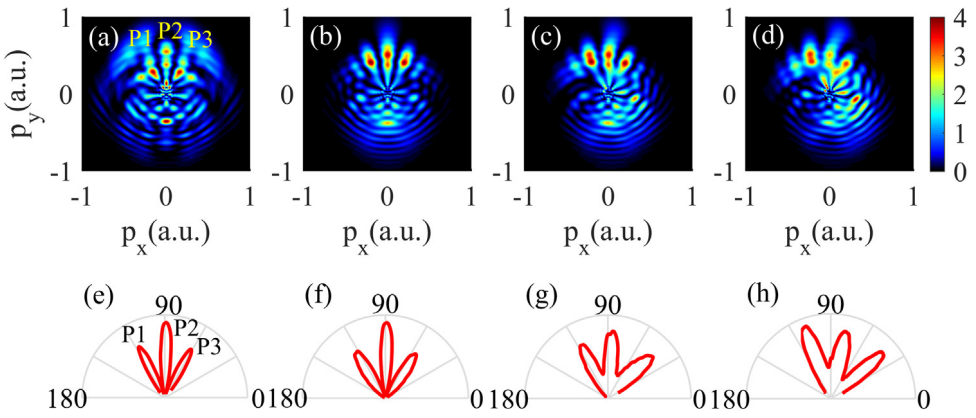

Fig. 1. The PMDs from argon atom. (a) The PMD with argon atom excited by only the linearly polarized IR pulse. (b), (c), and (d) Same as (a), but for argon atoms excited by both a linearly polarized IR pulse and an IAP. Here, The IR pulse and the IAP are temporally overlapped, and the ellipticity of the IAP are (b) $\varepsilon = 0$, (c) $\varepsilon = 0.5$, and (d) $\varepsilon = 1$, respectively. (e), (f), (g), and (h) The integrated signals for the PMDs shown in (a), (b), (c), and (d), respectively. The integrated range is between $|\mathbf{p}| = 0.15$ a.u. and $|\mathbf{p}| = 0.25$ a.u..

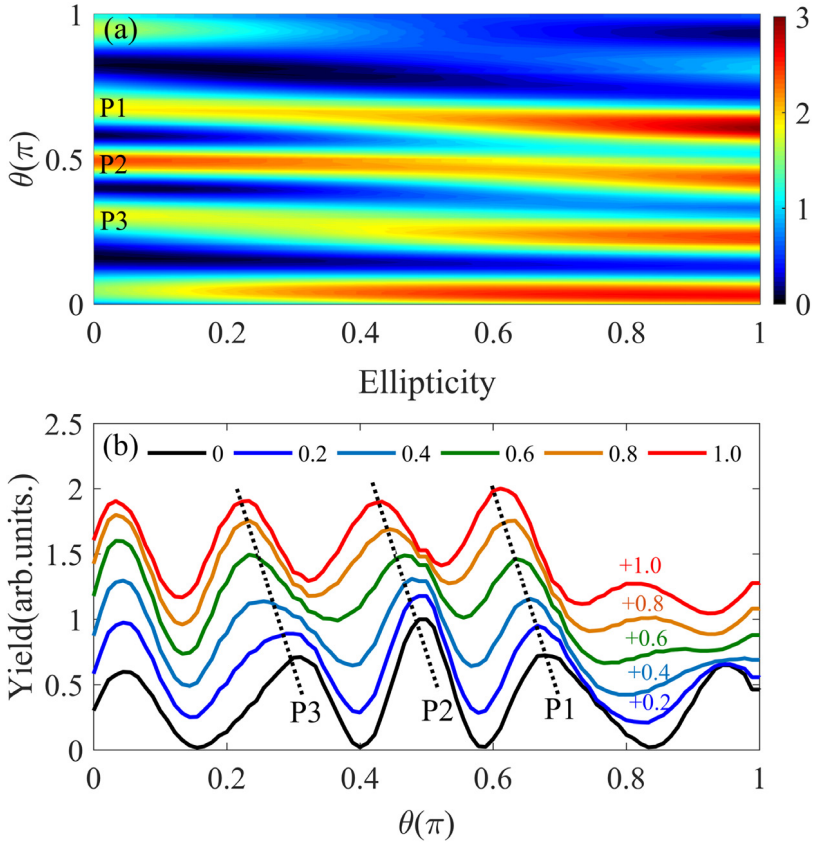

Fig. 2. (a) The photoelectron probability distribution as a function of the ellipticity of the IAP. The wavelengths of the IR pulse and the IAP are 800 nm and 79 nm, respectively. The intensities of the IR pulse and the IAP are 6×10^{13} W/cm^2 and 2×10^{12} W/cm^2, respectively. (b) The integrated signals of the PMDs. The yields of the photoelectron probability are shifted for clarity. The dash lines mark the shift of the main photoelectron probability peaks.

$a = 0.624$ for argon atom. The external laser field $\mathbf{E}(t)$ is combined by an IR ($\mathbf{E}_0(t)$) and an IAP ($\mathbf{E}_1(t)$) laser pulses. The IR pulse is linearly polarized and it is expressed as

$$\mathbf{E}_0(t) = E_0 f_0(t)\cos(\omega_0 t)\hat{y}. \tag{2}$$

$f_0(t)$ is the envelope of the IR pulse. The IR pulse has a sine square shape and its duration is four optical cycles. E_0 and ω_0 are the amplitude and frequency of the IR field, respectively. The wavelength of the IR pulse is 800 nm. The electric field of the IAP with the ellipticity ε is expressed as

$$\mathbf{E}_1(t) = \frac{1}{\sqrt{1+\varepsilon^2}} E_1 f_1(t)\sin(\omega_1 t)\hat{y} + \frac{\varepsilon}{\sqrt{1+\varepsilon^2}} E_1 f_1(t)\cos(\omega_1 t)\hat{x}. \tag{3}$$

$f_1(t)$ is the envelope of the IAP. The IAP has a sine square shape and its duration is four optical cycles. E_1 and ω_1 are the amplitude and frequency of the IAP field, respectively. The wavelength of the IAP is 79 nm. The IR pulse and the IAP are temporally overlapped.

We use the split-operator spectral method on a Cartesian grid to numerically solve the 2D-TDSE. Following [35], the electron wave function $\Psi(\mathbf{r}, t')$ at a given time t' is split into two parts:

$$\Psi(\mathbf{r}, t') = \Psi_{inner}(\mathbf{r}, t') + \Psi_{outer}(\mathbf{r}, t'), \tag{4}$$

where, $\Psi_{inner}(\mathbf{r}, t') = \Psi(\mathbf{r}, t')[1 - F_s(R_c)]$ represents the wave function in the inner region and it is propagated under the full Hamiltonian, and $\Psi_{outer}(\mathbf{r}, t') = \Psi(\mathbf{r}, t')F_s(R_c)$ stands for the wave function in the outer

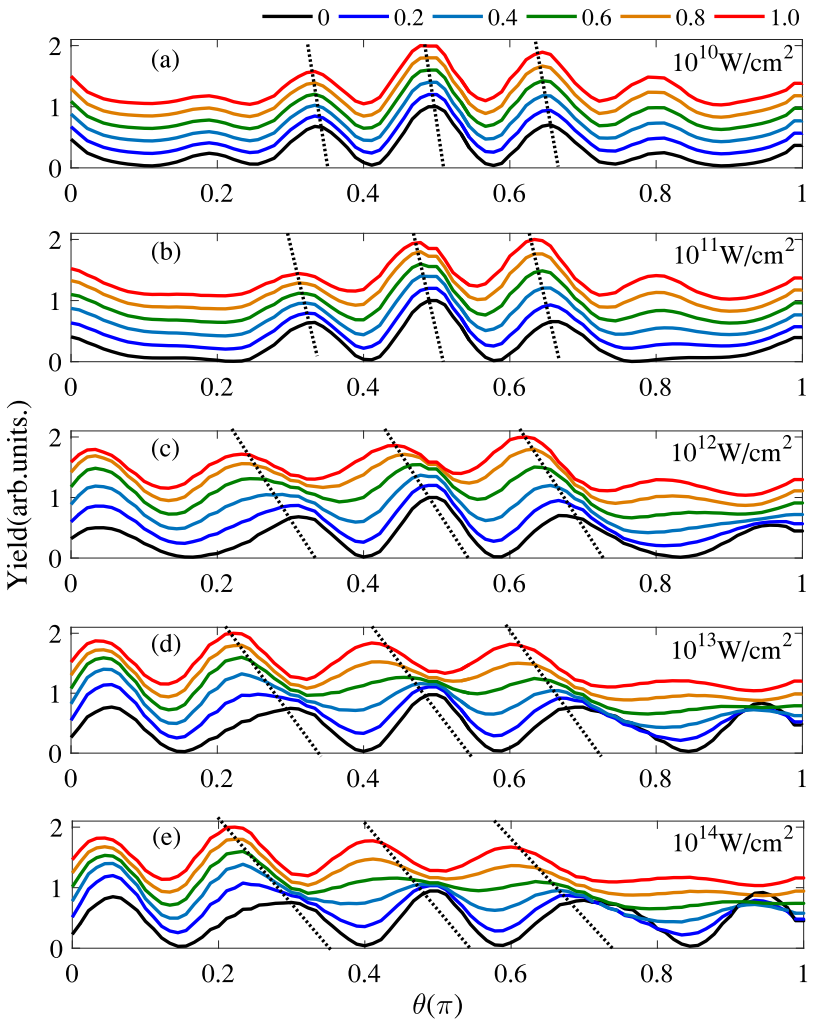

Fig. 3. The integrated signals of the PMDs. The wavelengths of the IR pulse and the IAP are 800 nm and 79 nm, respectively. The intensity of the IR pulse is 6×10^{13} W/cm^2. The intensities of the IAP are (a) 10^{10} W/cm^2, (b) 10^{11} W/cm^2, (c) 10^{12} W/cm^2, (d) 10^{13} W/cm^2, and (e) 10^{14} W/cm^2, respectively. The yields of the photoelectron probability with different intensities of the IAP are shifted for clarity. The dash lines mark the shift of the main photoelectron probability peaks.

region and it is propagated under the Volkov Hamiltonian analytically. Here, $F_s(R_c) = 1/(1+e^{-(r-R_c)/\Delta})$ is a split function that separates the whole space into the inner ($0 \longrightarrow R_c$) and outer ($R_c \longrightarrow R_{max}$) regions smoothly. Δ is the width of crossover region and R_c represents the boundary of inner space. In the present simulation, $\Psi_{outer}(\mathbf{r},t)$ is first transformed into momentum space,

$$\tilde{\Psi}^{p}_{outer}(\mathbf{p},t) = \int \Psi_{outer}(\mathbf{r},t)\frac{e^{-i[\mathbf{p}+\mathbf{A}(t)]\cdot\mathbf{r}}}{2\pi}d^2r, \tag{5}$$

where, $\mathbf{A}(t)$ is the vector potential of the laser pulse and $\tilde{\Psi}^{p}_{outer}(\mathbf{p},t)$ is the wave function in momentum space. Then we propagate $\tilde{\Psi}^{p}_{outer}(\mathbf{p},t)$ from time t to the end of the laser pulse as

$$\tilde{\Psi}^{f}_{outer}(\mathbf{p},t) = e^{-i\int_t^\infty \frac{1}{2}[\mathbf{p}+\mathbf{A}(t')]^2dt'}\tilde{\Psi}^{p}_{outer}(\mathbf{p},t), \tag{6}$$

where, $\tilde{\Psi}^{f}_{outer}(\mathbf{p},t)$ is the final wave function in momentum space ionized at time t. Finally, the PMD is obtained as

$$P(\mathbf{p},\infty) = \left|\int_t^\infty \tilde{\Psi}^{f}_{outer}(\mathbf{p},t)dt\right|^2. \tag{7}$$

3. Results and discussions

Fig. 1 shows the PMDs of argon ionized by different external laser fields. In the simulations of Fig. 1, the intensities of the IR pulse and the IAP are 6×10^{13} W/cm^2 and 2×10^{12} W/cm^2, respectively. The upper row is the two-dimensional PMDs. The lower row is the angular resolved photoelectron probability distributions, i.e. the integrated signals of the PMDs in the range of $|\mathbf{p}| \in [0.15\text{ a.u.}, 0.25\text{ a.u.}]$. Fig. 1(a) displays the PMD with the linearly polarized IR pulse alone. One can see that the PMD is symmetric with respect to $\mathbf{p}_x = 0$ a.u.. The PMD exhibits an arc-like structure and a clear fork-like structure in the angular range between $\pi/6$ and $5\pi/6$. The three main lobes of the fork-like structure are marked as P1, P2, and P3. Fig. 1(b) displays the PMD with the linearly polarized IR pulse combined with a linearly polarized IAP. Here, the polarization of the IAP is parallel to that of the IR pulse. In this case, the arc-like structure is tremendously suppressed and the fork-like structure becomes clearer. And the three main lobes P1, P2, and P3 are still symmetric with respect to $\mathbf{p}_x = 0$ a.u.. In Figs. 1(c) and (d), we show the PMDs driven by the combination of a linearly polarized IR pulse and an elliptical polarized IAP. The ellipticity of the IAP used in Figs. 1(c) and (d) are $\varepsilon = 0.5$ and 1, respectively. It is clear that the PMD is sensitive to the ellipticity of the IAP. The PMDs become clearly asymmetric and the angles of the three main lobes P1, P2, and P3 are shifted with increasing the ellipticity of the IAP. For clarity, the angular resolved integrated signals for the PMDs are presented in Figs. 1(e) – (h). Note that, only the peaks relative to the three main lobes P1, P2, and P3, i.e., the results within $[\pi/6, 5\pi/6]$ are shown in Figs. 1(e) – (h). One can see that the three main peaks rotate clockwise as the ellipticity of the IAP increases from $\varepsilon = 0$ to $\varepsilon = 1$ (see Figs. 1(f), (g), and (h)).

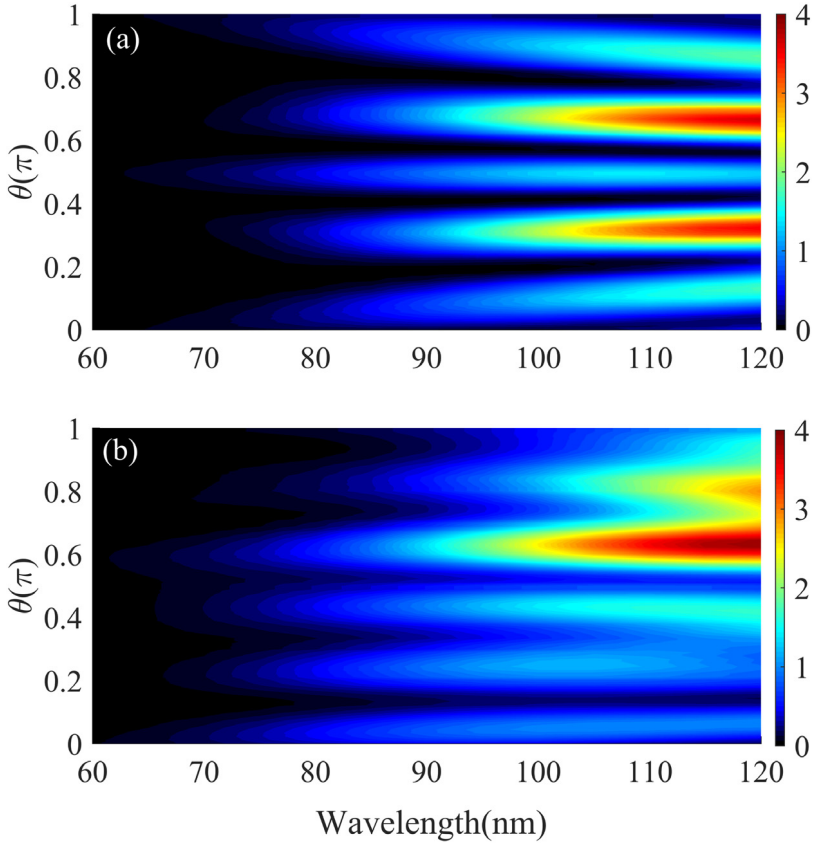

Fig. 4. The photoelectron probability distribution as a function of the wavelength of the IAP. The wavelength of the IR is 800 nm. The intensities of the IR pulse and the IAP are 6×10^{13} W/cm^2 and 2×10^{12} W/cm^2, respectively. The ellipticity of the IAP are (a) $\varepsilon = 0$ and (b) $\varepsilon = 1$.

In order to characterize the relationship between the PMD and the ellipticity of the IAP, we present the photoelectron probability distribution with the ellipticity of the IAP varied from $\varepsilon = 0$ to $\varepsilon = 1$ in Fig. 2(a). One can see more clearly that the photoelectron probability distribution shift as the ellipticity of the IAP increases. Fig. 2(b) shows the integrated signals of the PMDs and the integrated range is the same as that in Fig. 1. For the purpose of clarity, the normalized yield of the photoelectron momentum are shifted to avoid overlapping of different lines. One can see that the angle of the peak P2 is $\theta = 0.5\pi$ when the ellipticity of the IAP is $\varepsilon = 0$ (black solid line). It changes linearly and reaches $\theta = 0.42\pi$ as the ellipticity of the IAP changes from $\varepsilon = 0$ to $\varepsilon = 1$. Such a linear shift are also observed for the peaks P1 and P3. We fit the angular shift of the main peaks to a linear function $f(\varepsilon) = k\varepsilon(\pi) + \theta_0$ by using the least-squares method. Here $\varepsilon(\pi)$ and f represent the IAP ellipticity and the angular distribution of the main peaks, respectively. For the data shown in Fig. 2, the fitting parameters $k = -0.0780$, and $\theta_0 = 0.6800$ (P1), 0.5000 (P2), and 0.3070 (P3), respectively. The coefficient of determination (R-Squared) values are $R^2 = 0.9546$ (P1), 0.9192 (P2), and 0.9047 (P3), respectively. The larger value the better fits and 1 represents a perfect fit. As a result, the angular shift of the three main peaks can be used to characterize the ellipticity of the IAP.

The results above focus on the dependence of the PMD on the IAP ellipticity. Now, we investigate the influence of the IAP intensity and wavelength on the PMD. First, we calculate the PMDs with different intensities of the IAP. Fig. 3(a) – (e) show the results of the photoelectron probability distribution with the IAP intensities of 10^{10} W/cm^2, 10^{11} W/cm^2, 10^{12} W/cm^2, 10^{13} W/cm^2, and 10^{14} W/cm^2, respectively. In our calculation, the intensity of the IR pulse is fixed at 6×10^{13} W/cm^2. We find that the angular shift is not obvious when the IAP intensity is below 10^{10} W/cm^2. However, the main lobes present an obvious linear shift when the IAP intensity is above 10^{10} W/cm^2 and the slope of the fitted line gradually increases as the intensity of the IAP increases. One can see that the angular shift is measurable with the intensity of the IAP in a broad range from 10^{10} W/cm^2 to 10^{14} W/cm^2. In addition, the linear relationship between the angular shift and the ellipticity of the IAP always holds well.

Next, we calculate the PMDs with different wavelengths of the IAP. Fig. 4 shows the results of the photoelectron probability distribution with the IAP wavelength changes from 60 nm to 120 nm. The ellipticity of the IAP in Figs. 4(a) and (b) are $\varepsilon = 0$ and $\varepsilon = 1$, respectively. The intensities of the IR pulse and the IAP are 6×10^{13} W/cm^2 and 2×10^{12} W/cm^2, respectively. As shown in Fig. 4, the angles of the three main peaks of the photoelectron probability distribution can remain roughly stable as the IAP wavelength changes in a broad range. Especially in the wavelength range from 60 nm to 120 nm, where the IAP can be obtained in many laboratories, all the three main peaks do not shift with the IAP wavelength. Note that, similar results have also been observed with the IAP ellipticity ε within (0, 1) (not shown here). These results prove that the angles of the main peaks are independent on the wavelength of the IAP. As a result, this method for characterizing the ellipticity of an IAP can work well in a broad range of the IAP wavelength.

We finally test our method in a multicycle regime which is easily obtained in realistic experimental conditions. We have calculated the PMD with the duration of the IR laser pulse up to 35 optical cycles, and find the result is similar to that shown in Fig. 2. The most accurate measurement for the laser intensity has achieved 1% in experiment recently [36]. In our calculation, we have scanned the IR intensity jitter within ±5% which can be easily measured and controlled in experiment [36]. When the intensity of the IR pulse fluctuate in the range of ±5%, the angular distribution of the photoelectron probability remain stable. Meanwhile, to investigate the intensity averaging effect, we averaged the PMDs over the intensity distribution and find the intensity averaging effect will not prevent us from linear fitting the

angular shift of the main lobes. Moreover, we have also changed the CEP of the IR pulse within ±150 mrad, which can be easily obtained in experiment [37,38]. We find that the angular distribution of the photoelectron probability remain stable, too. Therefore, it is an advantage of our strategy because it does not need strictly requirement of the IR intensity and CEP stable.

For the IAP, on the other hand, it is important to carefully consider the CEP effect that maybe uncertainty in experiment [30,31]. However, the duration of the IAP relative to that of the IR pulse is too short to affect the PMD. In our calculation, to confirm this method works for arbitrary CEP of the IAP, we scan CEP of the IAP within $[0, 2\pi]$. Then we average the results of different CEPs to consider the CEP average effect. The calculations show that after averaging PMDs induced by different CEPs of the IAP, the angular distribution of the photoelectron probability still hold to that induced by the IAP's CEP = 0. Therefore, our method paves an efficient, simplified and robust way to characterize the ellipticity of the IAP.

4. Conclusion

In conclusion, we theoretically demonstrate a single-shot measurement method for characterizing the ellipticity of an IAP. By adding an attosecond XUV to a strong linearly polarized IR pulse, the ellipticity of the IAP has been encoded in the PMD. By measuring the angular shift of main photoelectron momentum lobes, the ellipticity of the IAP can be determined with only single-shot measurement.

Acknowledgments

This work was supported by the National Natural Science Foundation of China under Grants No. 11627809, 61475055, 11704137, 11404123 and the program for HUST Academic Frontier Youth Team.

References

[1] P.B. Corkum, F. Krausz, Attosecond science, Nat. Phys. 3 (2007) 381–387, http://dx.doi.org/10.1038/nphys620.
[2] H. Niikura, P.B. Corkum, Attosecond and Ångström science, Adv. At. Mol. Opt. Phys. 54 (2007) 511–548, http://dx.doi.org/10.1016/S1049-250X(06)54008-X.
[3] F. Krausz, M. Ivanov, Attosecond physics, Rev. Modern Phys. 81 (2009) 163, http://dx.doi.org/10.1103/RevModPhys.81.163.
[4] L. He, Q. Zhang, P. Lan, W. Cao, X. Zhu, C. Zhai, F. Wang, W. Shi, M. Li, X. Bian, P. Lu, A.D. Bandrauk, Monitoring ultrafast vibrational dynamics of isotopic molecules with frequency modulation of high-order harmonics, Nature Commun. 9 (2018) 1108, http://dx.doi.org/10.1038/s41467-018-03568-3.
[5] M. He, Y. Li, Y. Zhou, M. Li, W. Cao, P. Lu, Direct visualization of valence electron motion using strong-field photoelectron holography, Phys. Rev. Lett. 120 (2018) 133204, http://dx.doi.org/10.1103/PhysRevLett.120.133204.
[6] W. Liu, X. Li, Y. Song, C. Zhang, X. Han, H. Long, B. Wang, K. Wang, P. Lu, Cooperative enhancement of two-photon-absorption-induced photoluminescence from a 2D perovskite-microsphere hybrid dielectric structure, Adv. Funct. Mater. 28 (2018) 1707550, http://dx.doi.org/10.1002/adfm.201707550.
[7] J. Chen, K. Wang, H. Long, X. Han, H. Hu, W. Liu, B. Wang, P. Lu, Tungsten disulfide-gold nanohole hybrid metasurfaces for nonlinear metalenses in the visible region, Nano Lett. 18 (2018) 1344, http://dx.doi.org/10.1021/acs.nanolett.7b05033.
[8] L. He, P. Lan, A.-T. Le, B.N. Wang, B.C. Wang, X. Zhu, P. Lu, C.D. Lin, Real-time observation of molecular spinning with angular high-harmonic spectroscopy, Phys. Rev. Lett. 121 (2018) 163201, http://dx.doi.org/10.1103/PhysRevLett.121.163201.
[9] M. Hentschel, R. Kienberger, Ch. Spielmann, G.A. Reider, N. Milosevic, T. Brabec, P. Corkum, U. Heinzmann, M. Drescher, F. Krausz, Attosecond metrology, Nature 414 (2001) 509–513, http://dx.doi.org/10.1038/35107000.
[10] K. Zhao, Q. Zhang, M. Chini, Y. Wu, X. Wang, Z. Chang, Tailoring a 67 attosecond pulse through advantageous phase-mismatch, Opt. Lett. 37 (2012) 3891–3893, http://dx.doi.org/10.1364/OL.37.003891.
[11] E.J. Takahashi, P. Lan, O.D. Mücke, Y. Nabekawa, K. Midorikawa, Attosecond nonlinear optics using gigawatt-scale isolated attosecond pulses, Nature Commun. 4 (2013) 2691, http://dx.doi.org/10.1038/ncomms3691.
[12] J. Li, X. Ren, Y. Yin, K. Zhao, A. Chew, Y. Cheng, E. Cunningham, Y. Wang, S. Hu, Y. Wu, M. Chini, Z. Chang, 53-attosecond X-ray pulses reach the carbon K-edge, Nature Commun. 8 (2017) 186, http://dx.doi.org/10.1038/s41467-017-00321-0.
[13] T. Gaumnitz, A. Jain, Y. Pertot, M. Huppert, I. Jordan, F. Ardana-Lamas, H.J. Wörner, Streaking of 43-attosecond soft-X-ray pulses generated by a passively CEP-stable mid-infrared driver, Opt. Express 25 (2017) 27506–27518, http://dx.doi.org/10.1364/OE.25.027506.
[14] M. Uiberacker, Th. Uphues, M. Schultze, A.J. Verhoef, V. Yakovlev, M.F. Kling, J. Rauschenberger, N.M. Kabachnik, H. Schröder, M. Lezius, K.L. Kompa, H.-G. Muller, M.J.J. Vrakking, S. Hendel, U. Kleineberg, U. Heinzmann, M. Drescher, F. Krausz, Attosecond real-time observation of electron tunnelling in atoms, Nature 446 (2007) 627–632, http://dx.doi.org/10.1038/nature05648.
[15] J. Mauritsson, T. Remetter, M. Swoboda, K. Klünder, A. L'Huillier, K.J. Schafer, O. Ghafur, F. Kelkensberg, W. Siu, P. Johnsson, M.J.J. Vrakking, I. Znakovskaya, T. Uphues, S. Zherebtsov, M.F. Kling, F. Lépine, E. Benedetti, F. Ferrari, G. Sansone, M. Nisoli, Attosecond electron spectroscopy using a novel interferometric pump-probe technique, Phys. Rev. Lett. 105 (2010) 053001, http://dx.doi.org/10.1103/PhysRevLett.105.053001.
[16] D.D. Hickstein, F.J. Dollar, P. Grychtol, J.L. Ellis, R. Knut, C. Hernández-García, D. Zusin, C. Gentry, J.M. Shaw, T. Fan, K.M. Dorney, A. Becker, A. Jaroń-Becker, H.C. Kapteyn, M.M. Murnane, C.G. Durfee, Non-collinear generation of angularly isolated circularly polarized high harmonics, Nature Photon. 9 (2015) 743–750, http://dx.doi.org/10.1038/nphoton.2015.181.
[17] A. Fleischer, O. Kfir, T. Diskin, P. Sidorenko, O. Cohen, Spin angular momentum and tunable polarization in high-harmonic generation, Nature Photon. 8 (2014) 543–549, http://dx.doi.org/10.1038/nphoton.2014.108.
[18] B. Mahieu, S. Stremoukhov, D. Gauthier, C. Spezzani, C. Alves, B. Vodungbo, P. Zeitoun, V. Malka, G. De Ninno, G. Lambert, Control of ellipticity in high-order harmonic generation driven by two linearly polarized fields, Phys. Rev. A 97 (2018) 043857, http://dx.doi.org/10.1103/PhysRevA.82.033405.
[19] C. Hernández-García, C.G. Durfee, D.D. Hickstein, T. Popmintchev, A. Meier, M.M. Murnane, H.C. Kapteyn, I.J. Sola, A. Jaron-Becker, A. Becker, Schemes for generation of isolated attosecond pulses of pure circular polarization, Phys. Rev. A 93 (2016) 043855, http://dx.doi.org/10.1103/PhysRevA.93.043855.
[20] P.C. Huang, C. Hernández-García, J. Huang, P.Y. Huang, C. Lu, L. Rego, D.D. Hickstein, J.L. Ellis, A. Jaron-Becker, A. Becker, S. Yang, C.G. Durfee, L. Plaja, H.C. Kapteyn, M.M. Murnane, A.H. Kung, M. Chen, Polarization control of isolated high-harmonic pulses, Nature Photon. 12 (2018) 349–354, http://dx.doi.org/10.1038/s41566-018-0145-0.
[21] C. Zhai, X. Zhang, X. Zhu, L. He, Y. Zhang, B. Wang, Q. Zhang, P. Lan, P. Lu, Single-shot molecular orbital tomography with orthogonal two-color fields, Opt. Express 26 (2018) 2775–2784, http://dx.doi.org/10.1364/OE.26.002775.
[22] H. Yuan, L. He, F. Wang, B. Wang, X. Zhu, P. Lan, P. Lu, Tomography of asymmetric molecular orbitals with a one-color inhomogeneous field, Opt. Lett. 43 (2018) 931–934, http://dx.doi.org/10.1364/OL.43.000931.
[23] S. Luo, X. Ma, H. Xie, M. Li, Y. Zhou, W. Cao, P. Lu, Controlling nonsequential double ionization of Ne with parallel-polarized two-color laser pulses, Opt. Express 26 (2018) 13666–13676, http://dx.doi.org/10.1364/OE.26.013666.
[24] O. Kfir, P. Grychtol, E. Turgut, R. Knut, D. Zusin, D. Popmintchev, T. Popmintchev, H. Nembach, J.M. Shaw, A. Fleischer, H. Kapteyn, M. Murnane, O. Cohen, Generation of bright phase-matched circularly polarized extreme ultraviolet high harmonics, Nature Photon. 9 (2015) 99–105, http://dx.doi.org/10.1038/nphoton.2014.293.
[25] A.D. Bandrauk, J. Guo, K. Yuan, Circularly polarized attosecond pulse generation and applications to ultrafast magnetism, J. Opt. 19 (2017) 124016, http://dx.doi.org/10.1088/2040-8986/aa9673.
[26] D. Gui, L. Ji, A. Muhammad, W. Li, W. Cai, Y. Li, X. Li, X. Wu, P. Lu, Jahn–Teller effect on framework flexibility of hybrid organic–inorganic perovskites, J. Phys. Chem. Lett. 9 (2018) 751, http://dx.doi.org/10.1021/acs.jpclett.7b03229.
[27] C. Qin, L. Yuan, B. Wang, S. Fan, P. Lu, Effective electric-field force for a photon in a synthetic frequency lattice created in a waveguide modulator, Phys. Rev. A 97 (2018) 063838, http://dx.doi.org/10.1103/PhysRevA.97.063838.
[28] L. Xu, F. Li, S. Liu, F. Yao, Y. Liu, Low threshold plasmonic nanolaser based on graphene, Appl. Sci. 8 (2018) 2186, http://dx.doi.org/10.3390/app8112186.
[29] L. Xu, F. Li, L. Wei, J. Zhou, S. Liu, Design of surface plasmon nanolaser based on MoS_2, Appl. Sci. 8 (2018) 2110, http://dx.doi.org/10.3390/app8112110.
[30] P. He, C. Ruiz, F. He, Carrier-envelope-phase characterization for an isolated attosecond pulse by angular streaking, Phys. Rev. Lett. 116 (2016) 203601, http://dx.doi.org/10.1103/PhysRevLett.116.203601.
[31] S. Cui, P. He, F. He, Ionization of hydrogen atoms in attosecond pulse trains and strong infrared laser pulses, Phys. Rev. A 94 (2016) 053401, http://dx.doi.org/10.1103/PhysRevA.94.053401.
[32] C. Chen, Z. Tao, C. Hernández-García, P. Matyba, A. Carr, R. Knut, O. Kfir, D. Zusin, C. Gentry, P. Grychtol, O. Cohen, L. Plaja, A. Becker, A. Jaron-Becker, H. Kapteyn, M. Murnane, Tomographic reconstruction of circularly polarized high-harmonic fields: 3D attosecond metrology, Sci. Adv. 2 (2016) e1501333, http://dx.doi.org/10.1126/sciadv.1501333.
[33] Á. Jiménez-Galán, G. Dixit, S. Patchkovskii, O. Smirnova, F. Morales, M. Ivanov, Attosecond recorder of the polarization state of light, Nature Commun. 9 (2018) 850, http://dx.doi.org/10.1038/s41467-018-03167-2.
[34] L. Li, P. Lan, L. He, X. Zhu, J. Chen, P. Lu, Scaling law of high harmonic generation in the framework of photon channels, Phys. Rev. Lett. 120 (2018) 223203, http://dx.doi.org/10.1103/PhysRevLett.120.223203.

[35] S. Chelkowski, C. Foisy, A.D. Bandrauk, Electron-nuclear dynamics of multiphoton H_2^+ dissociative ionization in intense laser fields, Phys. Rev. A 57 (1998) 1176, http://dx.doi.org/10.1103/PhysRevA.57.1176.

[36] M.G. Pullen, W.C. Wallace, D.E. Laban, A.J. Palmer, G.F. Hanne, A.N. Grum-Grzhimailo, K. Bartschat, I. Ivanov, A. Kheifets, D. Wells, H.M. Quiney, X.M. Tong, I.V. Litvinyuk, R.T. Sang, D. Kielpinski, Measurement of laser intensities approaching 10^{15} W/cm^2 with an accuracy of 1%, Phys. Rev. A 87 (2013) 053411, http://dx.doi.org/10.1103/PhysRevA.87.053411.

[37] T. Wittmann, B. Horvath, W. Helml, M.G. Schätzel, X. Gu, A.L. Cavalieri, G.G. Paulus, R. Kienberger, Single-shot carrier–envelope phase measurement of few-cycle laser pulses, Nat. Phys. 5 (2009) 357, http://dx.doi.org/10.1038/nphys1250.

[38] B. Borchers, S. Koke, A. Husakou, J. Herrmann, G. Steinmeyer, Carrier-envelope phase stabilization with sub-10 as residual timing jitter, Opt. Lett. 36 (2011) 4146, http://dx.doi.org/10.1364/OL.36.004146.